

Entropic evidence for a Pomeranchuk effect in magic-angle graphene

<https://doi.org/10.1038/s41586-021-03319-3>

Received: 4 September 2020

Accepted: 29 January 2021

Published online: 7 April 2021

 Check for updates

Asaf Rozen^{1,4}, Jeong Min Park^{2,4}, Uri Zondiner^{1,4}, Yuan Cao^{2,4}, Daniel Rodan-Legrain², Takashi Taniguchi³, Kenji Watanabe³, Yuval Oreg¹, Ady Stern¹, Erez Berg¹✉, Pablo Jarillo-Herrero²✉ & Shahal Ilani¹✉

In the 1950s, Pomeranchuk¹ predicted that, counterintuitively, liquid ³He may solidify on heating. This effect arises owing to high excess nuclear spin entropy in the solid phase, where the atoms are spatially localized. Here we find that an analogous effect occurs in magic-angle twisted bilayer graphene^{2–6}. Using both local and global electronic entropy measurements, we show that near a filling of one electron per moiré unit cell, there is a marked increase in the electronic entropy to about $1k_B$ per unit cell (k_B is the Boltzmann constant). This large excess entropy is quenched by an in-plane magnetic field, pointing to its magnetic origin. A sharp drop in the compressibility as a function of the electron density, associated with a reset of the Fermi level back to the vicinity of the Dirac point, marks a clear boundary between two phases. We map this jump as a function of electron density, temperature and magnetic field. This reveals a phase diagram that is consistent with a Pomeranchuk-like temperature- and field-driven transition from a low-entropy electronic liquid to a high-entropy correlated state with nearly free magnetic moments. The correlated state features an unusual combination of seemingly contradictory properties, some associated with itinerant electrons—such as the absence of a thermodynamic gap, metallicity and a Dirac-like compressibility—and others associated with localized moments, such as a large entropy and its disappearance under a magnetic field. Moreover, the energy scales characterizing these two sets of properties are very different: whereas the compressibility jump has an onset at a temperature of about 30 kelvin, the bandwidth of magnetic excitations is about 3 kelvin or smaller. The hybrid nature of the present correlated state and the large separation of energy scales have implications for the thermodynamic and transport properties of the correlated states in twisted bilayer graphene.

Systems of strongly interacting fermions exhibit competition between localization, which minimizes the potential energy, and itinerancy, which minimizes the kinetic energy. The advent of two-dimensional moiré systems, such as magic-angle twisted bilayer graphene^{2–6} (MATBG), allows this physics to be studied by controlling the ratio between the electronic interactions and bandwidth in a highly tunable way. When this ratio is large, electrons tend to localize and form Mott insulators^{7,8}. When the bandwidth dominates, a Fermi liquid state is formed in which electrons are itinerant. MATBG is at the boundary between these two extremes, showing a host of fascinating electronic phases, including correlated insulators^{3,9,10}, Chern insulators^{11–13}, superconductors^{4,9,10} and ferromagnets^{14,15}. Scanning tunnelling spectroscopy^{16–19} and electronic compressibility measurements^{20,21} indicate that in this system the strengths of the Coulomb interaction and the kinetic energy are indeed comparable. In this regime, there is an inherent tension between localized and itinerant descriptions of the physics. Moreover, the topological

character^{22–24} of the nearly-flat bands in MATBG implies that a simple ‘atomic’ description, in which electrons are localized to individual moiré lattice sites, may not be appropriate. Instead, a picture analogous to that of quantum Hall ferromagnetism has been proposed^{25–27}. Understanding this interplay between itinerancy and localization, and the new physics that emerges from it, remains a major challenge.

In this work we find that, surprisingly, the correlated state in MATBG above a filling of one electron per moiré site has a hybrid nature, with some properties resembling those of an itinerant system, and others resembling those of localized electrons. At temperatures of a few kelvin we measure unusually large excess entropy, which is rapidly suppressed by a moderate in-plane magnetic field. This suggests that even at such low temperatures, there are strongly fluctuating magnetic moments in the system, a behaviour typically associated with local moments. On the other hand, our measurements find that this state is metallic and has no thermodynamic gap, naturally fitting an itinerant picture.

¹Department of Condensed Matter Physics, Weizmann Institute of Science, Rehovot, Israel. ²Department of Physics, Massachusetts Institute of Technology, Cambridge, MA, USA. ³National Institute for Materials Science, Tsukuba, Japan. ⁴These authors contributed equally: Asaf Rozen, Jeong Min Park, Uri Zondiner, Yuan Cao. ✉e-mail: eretz.berg@weizmann.ac.il; pjarillo@mit.edu; shahal.ilani@weizmann.ac.il

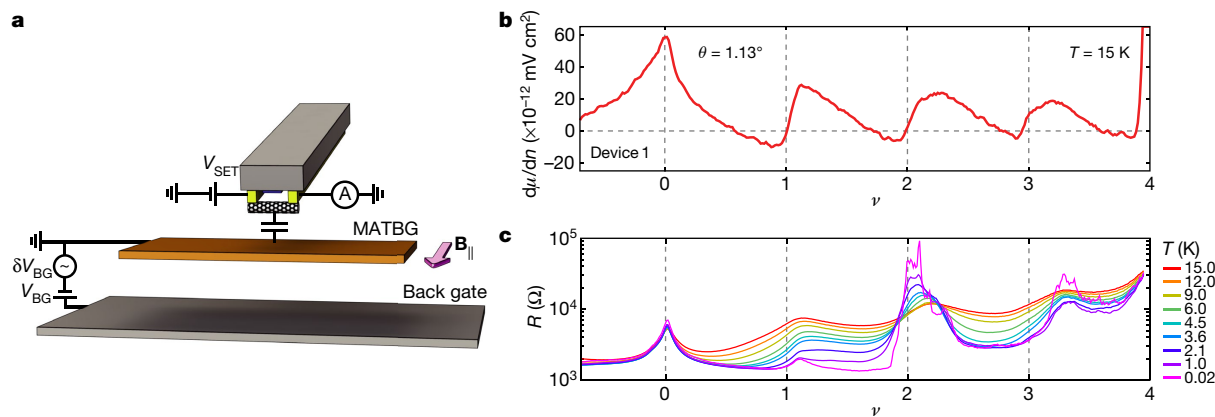


Fig. 1 | Experimental setup and device characterization. **a**, A nanotube-based single electron transistor (SET) is used to measure the local electronic compressibility and entropy of magic-angle twisted bilayer graphene (MATBG). The MATBG is encapsulated between top and bottom h-BN layers (not shown) and has a metallic back gate. By monitoring the current through the SET, we track changes in the MATBG chemical potential, $d\mu$, in response to a density modulation, dn , produced by an a.c. voltage on the back gate 21 , δV_{BG} . A d.c. back-gate voltage, V_{BG} , sets the overall carrier density in the MATBG, n . Some of the measurements are performed in a parallel magnetic field, $B_{||}$ (indicated). **b**, Inverse compressibility, $d\mu/dn$, measured as a function of the moiré lattice filling factor, $\nu = n/(n_s/4)$, at $T = 15$ K (n_s is the density that corresponds to four electrons per moiré site). Measurements are done on a large spatial domain ($5 \mu\text{m} \times 4 \mu\text{m}$) throughout which the twist angle is extremely homogenous, $\theta = 1.130^\circ \pm 0.005^\circ$ (measured by spatial mapping of

the V_{BG} that corresponds to n_s , as in refs. 21,41). As seen previously 21 , a jump of $d\mu/dn$ appears near all integer filling factors. This jump corresponds to a Fermi surface reconstruction, in which some combination of the spin/valley flavours filling is reset back to near the charge neutrality point, and correspondingly $d\mu/dn$ shows a cascade of sawtooth features as a function of density. The trace is measured at $T = 15$ K, showing that even at this high temperature this sawtooth cascade is well developed. **c**, Two-probe resistance, R , measured as a function of ν and temperature (see key). Notice that unlike the inverse compressibility, which measures a local quantity, the resistance gives an averaged result over domains with different twist angle. Therefore, the resistance maxima are slightly shifted from the usual integer ν values, probably because another domain with a small difference in twist angle dominates the transport characteristics globally.

The presence of fluctuating moments at temperatures much below the electronic bandwidth indicates the existence of a new, anomalously small energy scale associated with the bandwidth of magnetic excitations, which is an order of magnitude smaller than the scale where a jump appears in the compressibility 21,28 . This jump marks the boundary between the new state at filling factor $\nu > +1$ and the state at lower densities. By tracking the dependence of this boundary on temperature and magnetic field, we find that it exhibits an electronic analogue $^{29-32}$ of the Pomeranchuk effect 1 in ^3He . In that system, a transition from a Fermi liquid to a solid occurs on increasing the temperature, driven by the high nuclear spin entropy of the atoms in the solid. Similarly, we find that the new state above $\nu = +1$ is favoured relative to the metallic state at $\nu < +1$ on raising the temperature, owing to the former's high magnetic entropy. The transition near $\nu = +1$ can also be driven by an in-plane magnetic field that polarizes the free moments. (A related effect near $\nu = -1$ was proposed very recently, on the basis of transport measurements 33 .) The hybrid state observed here, with itinerant electrons coexisting with strongly fluctuating magnetic moments, calls for a new understanding of electron correlations in MATBG.

Our data are measured using two independent techniques on two conceptually different devices. The bulk of the results are obtained from local measurements of the electronic entropy 34,35 and compressibility using a scanning nanotube single-electron transistor (SET) that probes a hexagonal boron nitride (hBN)-encapsulated MATBG device (device 1, Fig. 1a). We focus on a large ($5 \mu\text{m} \times 4 \mu\text{m}$) region with an extremely homogenous twist angle that is close to the theoretical magic angle $\theta = 1.130^\circ \pm 0.005^\circ$. Similar results are obtained from global entropy measurements using a monolayer graphene sensor (device 2; see section 'Global measurements of the entropy'). Both methods have been described elsewhere 21,36 .

Electronic compressibility and transport

The inverse compressibility, $d\mu/dn$, measured in device 1 at $T = 15$ K as a function of the filling factor, $\nu = n/(n_s/4)$ (where μ is the chemical

potential, n is the carrier density, and n_s corresponds to four electrons per moiré superlattice unit cell), is shown in Fig. 1b. As reported previously 21 , sharp jumps in $d\mu/dn$ are observed close to integer values of ν , reflecting Fermi surface reconstructions. These were termed Dirac revivals as they were interpreted as resets of partially filled energy bands back to near the Dirac point, leading to the decreased compressibility. The cascade of revivals is already very prominent at this relatively high temperature. Measurements of the two probe resistance, R , versus ν at various temperatures T (Fig. 1c) show insulating behaviour at $\nu = 2, 3$ and semi-metallic behaviour at $\nu = 0$. As previously noted 37 , R shows a step-like increase across $\nu \approx 1$, which gradually disappears with decreasing temperature, very different to the behaviour at other integer values of ν .

The unusual physics near $\nu = 1$ is revealed by the dependence of $d\mu/dn$ on T and parallel magnetic field, $B_{||}$. At low temperature and $B_{||} = 0$ T (Fig. 2a), the jump in $d\mu/dn$ occurs at ν slightly larger than 1. Increasing the temperature moves the jump towards lower ν , and surprisingly, increases the magnitude of the jump rather than smearing it. Similar measurements with $B_{||} = 12$ T at low T (Fig. 2b) show a much larger jump, which is also closer to $\nu = 1$. With increasing temperature, this jump remains close to $\nu = 1$, but in contrast to the $B_{||} = 0$ T case, its amplitude is reduced and its width increased.

Local measurements of electronic entropy

The chemical potential, $\mu(\nu, T)$ (measured relative to that at charge neutrality), can be obtained by integrating $d\mu/dn$ over carrier density (Fig. 2c, d). Visibly, μ depends strongly on T for a range of values of ν . This is clearly seen when we plot μ versus T at two representative ν values (Fig. 2c, inset). At $\nu = 0.2$, μ is practically independent of T (blue). In contrast, at $\nu = 0.9$ (red) μ is nearly constant until $T \approx 4$ K, and then decreases approximately linearly with T . At $\nu > 1.15$, μ is again nearly temperature independent. Comparison of μ at $B_{||} = 0$ T (Fig. 2c) with that at $B_{||} = 12$ T (Fig. 2d) reveals a clear contrast: whereas for $B_{||} = 0$ T, μ is a decreasing function of temperature for $0.4 < \nu < 1.15$, for $B_{||} = 12$ T, μ decreases with T for $\nu < 0.9$ and increases for $\nu > 0.9$.

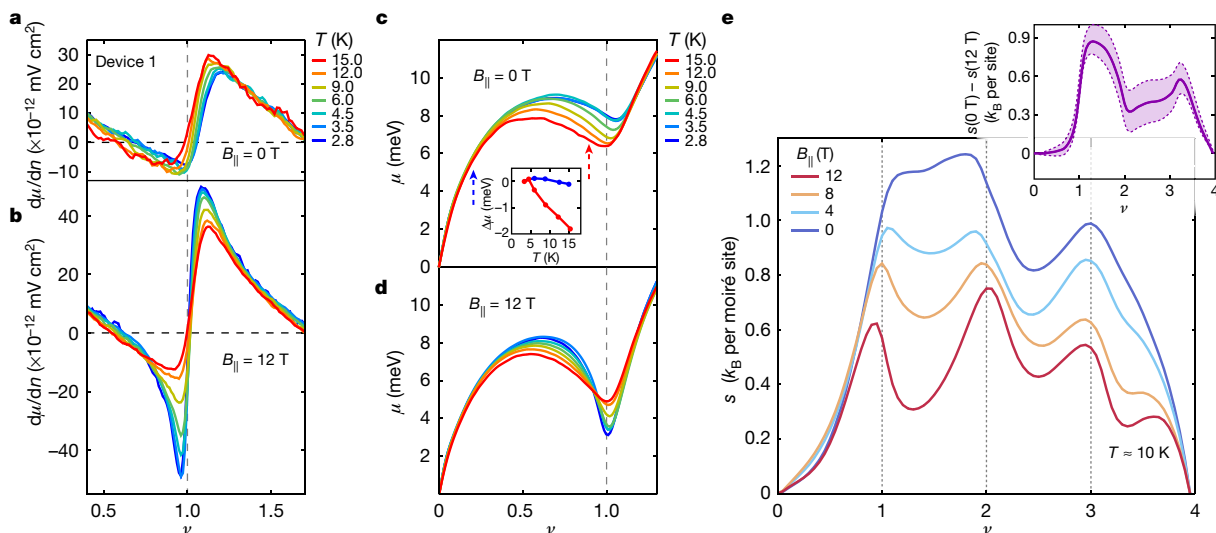


Fig. 2 | Measurement of large magnetic entropy above $\nu=1$. **a**, Inverse compressibility, $d\mu/dn$, as a function of ν , near $\nu=1$, measured at zero parallel magnetic field, $B_{||} = 0$ T, and at several temperatures (see key). With increasing T , the jump in $d\mu/dn$ moves towards lower ν and becomes stronger. **b**, Same measurement as **a** but done at $B_{||} = 12$ T. Here, opposite to the zero-field case, increasing T reduces the magnitude of the $d\mu/dn$ jump, as expected from thermal smearing. **c**, The chemical potential μ (relative to that of the charge neutrality point) versus ν at $B_{||} = 0$ T, obtained by integrating the $d\mu/dn$ signal in **a** with respect to n . Inset, $\Delta\mu$ (defined as $\mu(T, \nu) - \mu(T = 2.8$ K, $\nu)$) as a function of temperature for $\nu = 0.2$ (blue) and $\nu = 0.9$ (red). At $\nu = 0.2$ the chemical potential is nearly temperature independent, whereas at $\nu = 0.9$ it is roughly constant until $T \approx 4$ K and then starts decreasing approximately linearly with T . **d**, Similar to **c** but at $B_{||} = 12$ T. In contrast to the zero-field case, here, below $\nu \approx 0.9$, μ decreases with T while above $\nu \approx 0.9$, μ increases with T . **e**, The electronic entropy s (in units of k_B per moiré unit cell) as a function of ν at $T \approx 10$ K and at various parallel magnetic fields, $B_{||} = 0, 4, 8, 12$ T (see key). To obtain the entropy we determine the partial derivative $(\partial\mu/\partial T)_{\nu, B_{||}}$ from a linear fit to the measured μ versus T in the range $T = 4.5$ – 15 K. The entropy per moiré cell is then obtained by integrating Maxwell's relation, $(\partial s/\partial\nu)_{T, B_{||}} = -(\partial\mu/\partial T)_{\nu, B_{||}}$ over ν (see Supplementary Information for details). At $B_{||} = 0$, the entropy climbs rapidly near $\nu = 1$ to a value of about $1.2k_B$ per moiré cell. Inset, the difference between the entropies at low and high fields, $s(B_{||} = 0$ T) $-$ $s(B_{||} = 12$ T). The purple shading shows the estimated standard deviation due to the measurement accuracy.

These measurements allow us to directly determine the entropy of the system, by integrating Maxwell's relation, $(\frac{\partial s}{\partial\nu})_T = -(\frac{\partial\mu}{\partial T})_\nu$, to obtain $s(\nu, T)$ (where s is the entropy per moiré unit cell). For more details on this procedure, see Supplementary Information section 1. Figure 2e shows $s(\nu)$ at $T \approx 10$ K (obtained from the slope of μ versus T in the range $T = 4.5$ – 15 K), for $B_{||} = 0$ T, 4 T, 8 T and 12 T. At $B_{||} = 0$ T, the entropy is small at low ν , climbs close to $\nu \approx 1$, remains roughly constant between $\nu \approx 1$ and 2 at $s \approx 1.2k_B$, drops rapidly near $\nu \approx 2$, and decreases towards zero after $\nu \approx 3$. Clearly, the ν dependence of the entropy is qualitatively different from that of the compressibility: whereas the latter drops sharply near $\nu \approx 1$ (Fig. 2a), the former remains at a high value.

An important insight into the origin of this large entropy is given by its magnetic field dependence. As seen in Fig. 2e, the entropy above $\nu \approx 1$ depends strongly on $B_{||}$. In particular, at $B_{||} = 12$ T, most of the entropy between $\nu \approx 1$ and 2 is quenched. The inset shows $s(B_{||} = 0$ T) $-$ $s(B_{||} = 12$ T) versus ν (the purple shading indicates error bars; see Supplementary Information section 1). The entropy difference increases sharply near $\nu \approx 1$, reaching a maximum of $(0.85 \pm 0.1)k_B$ between $\nu \approx 1$ and 2. To appreciate the importance of this value, we recall that an entropy of $k_B \ln 2 \approx 0.7k_B$ corresponds to two degenerate states on each moiré unit cell. Moreover, in a Fermi liquid, we would expect a much weaker change of the entropy with $B_{||}$ (see Supplementary Information section 4), of the order of k_B times the ratio of the Zeeman energy (about 1 meV at $B_{||} = 12$ T) to the bandwidth, estimated to be $W \approx 30$ meV (see below). Finally, we observe that at $B_{||} = 12$ T the entropy shows a cascade of drops following each integer ν . These drops are similar to the revival drops observed in the compressibility (Supplementary Information section 5) and are reproduced by mean-field calculations (Supplementary Information section 3). The strong quenching of entropy by moderate $B_{||}$ strongly suggests a magnetic origin.

Global measurements of the entropy

To test the robustness of our results, we measured the entropy in a completely different setup, in which a sheet of monolayer graphene senses the chemical potential of MATBG, averaged over the entire device³⁶ (Fig. 3a). Figure 3b shows the entropy extracted in three different temperature ranges. We see (inset) that the globally measured entropy for $T = 4$ – 16 K is in good agreement with the locally measured one over a similar range of temperatures, both in the overall shape, the magnitude of $s(\nu)$, and the detailed features. At elevated temperatures, the minimum in the entropy at $\nu = 0$ gradually fills in, evolving from a double-dome structure at low T (corresponding to the valence and conduction flat bands) to a single dome at high T . This dependence is qualitatively reproduced by a naive calculation for a system of non-interacting electrons, whose density of states rises linearly from the charge neutrality point until the band edges (Fig. 3c). The merging of the domes in $s(\nu)$ occurs when the temperature exceeds a fraction of the bandwidth. Calibrating the bandwidth using the measured entropy at $T \approx 55$ K gives $W \approx 30$ meV (where W is the full bandwidth—from valence band bottom to conduction band top), in rough agreement with scanning tunnelling microscopy^{16–19} and compressibility³⁶ experiments. This free-electron picture is of course invalid at low temperatures, where interactions are important. The measured $s(\nu)$ in the valence band is approximately a mirror image of $s(\nu)$ in the conduction band (Fig. 3b), although it is smaller and has less pronounced features. This is consistent with the weaker $d\mu/dn$ revivals observed in the valence band relative to the conduction band^{21,36} (Supplementary Information section 9).

Mapping the phase diagram

So far, we have shown the change in the magnetic entropy and compressibility near $\nu = 1$. This change may be due to a continuous build-up

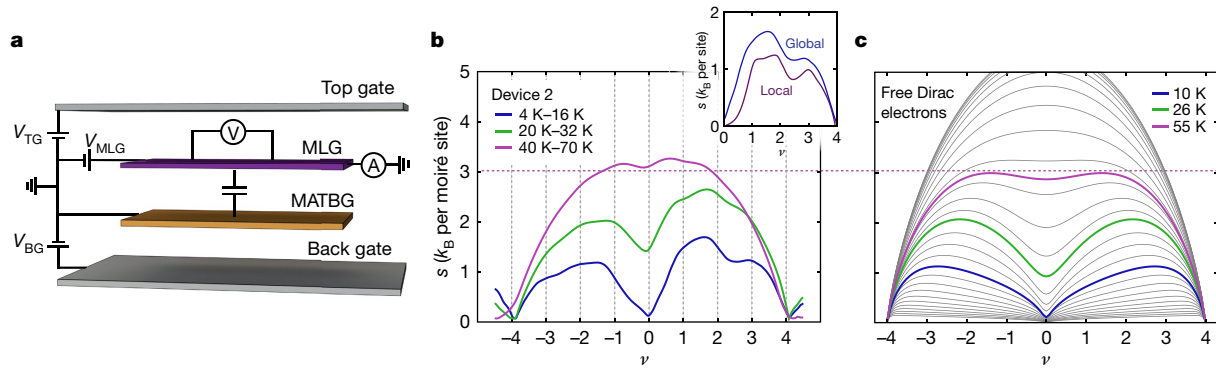


Fig. 3 | Temperature dependence of the entropy. **a**, Experimental setup for measuring the global entropy, averaged over the entire device³⁶. The device consists of MATBG and a monolayer graphene (MLG) sensor layer, separated by an ultrathin (1 nm) layer of h-BN (not shown), as well as top and back metallic gates. By balancing the electrochemical potential of the adjacent layers in the device, we can obtain the relationship between the carrier density and chemical potential of MATBG and MLG and the gate voltages applied to the system (top-gate voltage, V_{TG} ; back-gate voltage, V_{BG}). In the special case where the carrier density of MLG is zero, tuned by V_{MLG} , that is, at its charge neutrality point, the chemical potential of MATBG is directly proportional to the voltage applied to the top gate. This technique allows us to reliably extract the chemical potential and entropy of MATBG at temperatures up to 70 K. **b**, The measured entropy, in units of k_B per moiré unit cell, as a function of ν at three different temperature ranges (see key). The entropy derivative, $ds/d\nu$, is obtained from a linear fit to μ versus T in the corresponding temperature range, and is then

integrated over ν to yield the entropy per moiré unit cell (similar to Fig. 2e). Inset, comparison between the ν dependence of the entropy, measured at the low temperature range, as obtained from local and global measurements. **c**, The entropy as a function of ν and T calculated for a system of four degenerate non-interacting Dirac bands (whose density of states climbs linearly with energy from the Dirac point to the end of the conduction or the valence band). The colour-coded lines (see key) show the curves whose temperatures correspond to the mean of the temperature ranges of the experimental curves. The grey lines represent the entire evolution from zero temperature to high temperature, where the entropy saturates at a value of $8\ln 2 \approx 5.5$, where the factor 8 reflects the total number of energy bands. A bandwidth of $W = 30$ meV is chosen such that the calculated value of the entropy at the highest temperature roughly matches the one obtained from the measured curve at the same temperature.

of electronic correlations. Alternatively, it could be interpreted as an underlying first-order phase transition between two distinct phases. Naively, one would then expect a discontinuous jump in thermodynamic properties and hysteretic behaviour across the transition, which are not observed. However, we note that a true first-order phase transition is forbidden in two dimensions in the presence of disorder or long-range Coulomb interactions³⁸, as these broaden the transition into a mesoscale coexistence region (Supplementary Information section 10). Experimentally, although the revival transition is very sharp and may be consistent with a Coulomb- and/or disorder- smeared first-order transition, we cannot rule out a sharp crossover or a higher-order phase transition. Nevertheless, the sharpness of the rise of $d\mu/dn$ at the revival transition allows us to precisely track its filling factor, $\nu = \nu_R$ (Fig. 4a), and map a phase diagram, which is naturally explained when this feature is interpreted as a proxy for a first-order transition.

The measured ν_R versus $B_{||}$ and T forms a surface in $(\nu, B_{||}, T)$ space (Fig. 4b), whose projections onto the $(\nu, B_{||})$ and (ν, T) planes are shown in Fig. 4c, d. At $T = 2.8$ K and at low $B_{||}$, ν_R depends weakly on $B_{||}$, but decreases linearly above $B_{||} \approx 4$ T (Fig. 4c, blue). A similar crossover is observed at higher temperatures, but with a crossover $B_{||}$ that increases with temperature. The T dependence of ν_R at $B_{||} = 0$ T (Fig. 4d) is linear at low temperatures and curves up at higher temperatures. As $B_{||}$ increases, the curve shifts towards smaller values of ν , and simultaneously its slope at low temperatures changes sign. At $B_{||} = 12$ T, ν_R first increases with T , reaches a maximum at $T \approx 9$ K, and then decreases.

The phenomenology seen in Fig. 4b–d can be understood in terms of a first-order phase transition at $\nu = \nu_R$ between a Fermi liquid phase below ν_R , and a ‘free moment’ phase above it. The latter has a high concentration of free moments (about one per moiré site), coexisting with a low density of itinerant electrons. Within this framework, the shift of ν_R as a function of $B_{||}$ and T reflects the magnetization and entropy differences between the two neighbouring phases.

At $B_{||} = 0$ T, the free moment phase has a higher entropy than the Fermi liquid, owing to thermal fluctuations of the moments. Hence, the former becomes entropically favourable at high temperatures.

This explains the observed decrease of ν_R with increasing T at low fields (Fig. 4d). Raising the temperature at fixed ν may therefore drive a transition from the Fermi liquid to the free moments phase, an electronic analogue of the Pomeranchuk effect. As $B_{||}$ increases and the Zeeman energy exceeds the temperature, the moments become nearly fully polarized and their entropy is quenched (as is observed directly in Fig. 2e). Consequently, at low temperatures and sufficiently high fields, the Fermi liquid phase is favoured by raising the temperature. The trend reverses once the temperature exceeds the Zeeman energy. This explains the non-monotonic behaviour of ν_R as a function of T , seen at $B_{||} = 12$ T in Fig. 4d. The main features of the phase boundary are qualitatively reproduced in a thermodynamic model of the two phases (Supplementary Information section 7, and insets of Fig. 4b–d). Note that the experiment probes moments that couple to an in-plane field. This includes Zeeman-coupled spins and may also include the valleys if their in-plane orbital moment is non-zero.

Discussion

The observation of free magnetic moments at surprisingly low temperatures has profound implications for the physics of MATBG. Low-energy magnetic fluctuations are destructive for superconductivity, and may be the limiting factor for the superconducting transition temperature. Moreover, increased scattering from fluctuating moments can account for the ‘strange metal’ behaviour reported over a broad range of temperatures^{39,40}.

An important question raised by our observations concerns the origin of the free moments. Soft collective modes have been predicted in insulating states of MATBG^{25–27}, but our experiments show metallic behaviour near $\nu = 1$. Moreover, the energy scale associated with the appearance of free moments is strikingly low (3 K or less), much below the microscopic energy scales in the system. Understanding the state near $\nu = 1$, which combines behaviours associated with electron localization and itinerancy, and its surprisingly low onset temperature, poses an important challenge for the theory of MATBG.

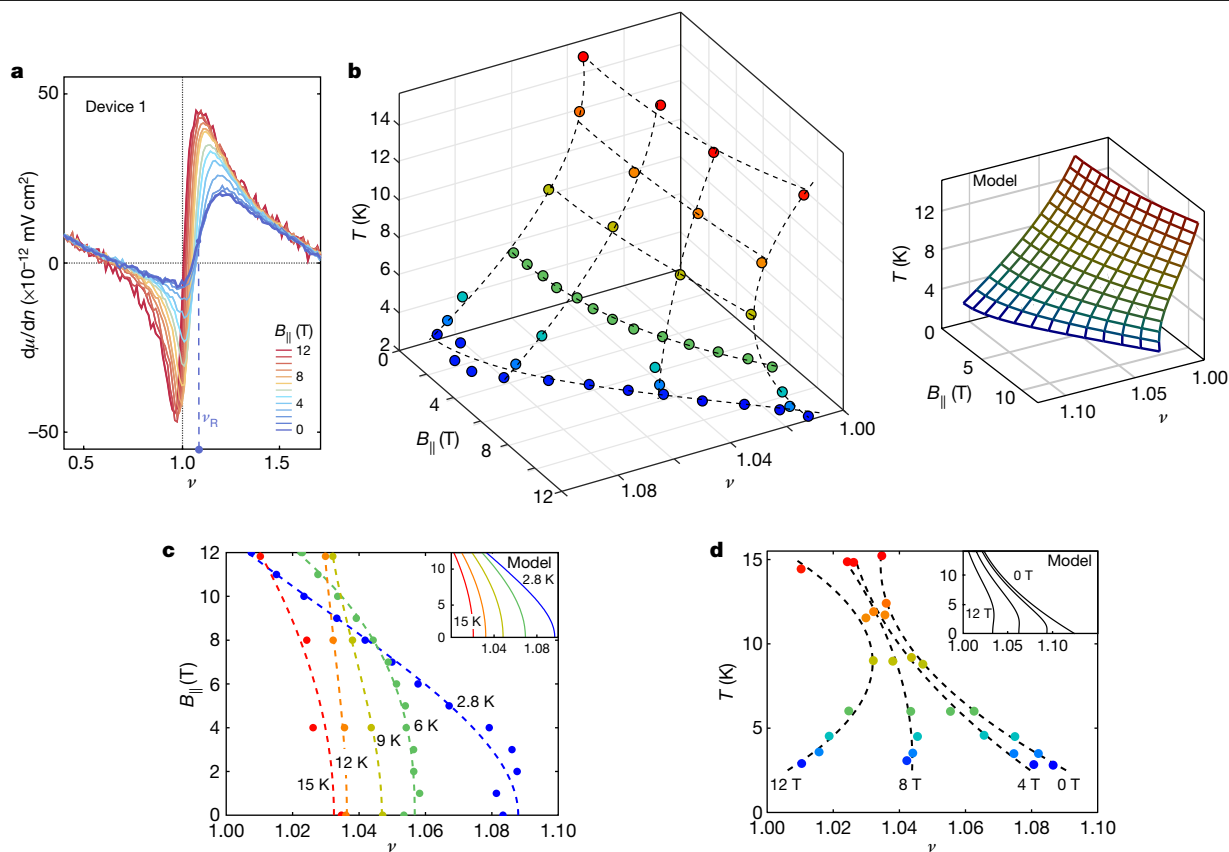


Fig. 4 | Experimental phase diagram. **a**, The inverse compressibility, $d\mu/dn$, measured as a function of ν near $\nu=1$, at several values of parallel magnetic field, $B_{||}$. We track the filling factor that corresponds to the centre of the jump in $d\mu/dn$ (labelled ν_R). The application of $B_{||}$ is seen to push ν_R to lower values. **b**, Left panel, measured ν_R as a function of $B_{||}$ and T , plotted as dots in $(\nu, B_{||}, T)$ space (the dots are coloured by their temperature as in **c**; the dashed lines are polynomial fits to the dots at constant $B_{||}$ or constant T). Right panel, the same surface calculated from a simple model that assumes a transition between a Fermi liquid and a metallic phase that contains one free moment per moiré site

(see text). **c**, Projection of the data in **b** onto the $(\nu, B_{||})$ plane, showing the dependence of ν_R on $B_{||}$ for various temperatures. At low fields, ν_R is independent of field but becomes linear in $B_{||}$ at high fields, a behaviour expected from the field polarization of free moments (see text). Inset, curves calculated from the model. **d**, Projection onto the (ν, T) plane, showing the dependence of ν_R on T for various magnetic fields. At $B_{||} = 0$ T, ν_R is linear in T at small values of T and then curves up at higher values of T . At high magnetic field, the dependence of ν_R on T becomes non-monotonic. Inset, curves calculated from the model.

Online content

Any methods, additional references, Nature Research reporting summaries, source data, extended data, supplementary information, acknowledgements, peer review information; details of author contributions and competing interests; and statements of data and code availability are available at <https://doi.org/10.1038/s41586-021-03319-3>.

1. Pomeranchuk, I. On the theory of He³. *Zh. Eksp. Teor. Fiz* **20**, 919 (1950).
2. Bistritzer, R. & MacDonald, A. H. Moiré bands in twisted double-layer graphene. *Proc. Natl Acad. Sci. USA* **108**, 12233–12237 (2011).
3. Cao, Y. et al. Correlated insulator behaviour at half-filling in magic-angle graphene superlattices. *Nature* **556**, 80–84 (2018).
4. Cao, Y. et al. Unconventional superconductivity in magic-angle graphene superlattices. *Nature* **556**, 43–50 (2018).
5. Li, G. et al. Observation of Van Hove singularities in twisted graphene layers. *Nat. Phys.* **6**, 109–113 (2010).
6. Suárez Morell, E., Correa, J. D., Vargas, P., Pacheco, M. & Barticevic, Z. Flat bands in slightly twisted bilayer graphene: tight-binding calculations. *Phys. Rev. B* **82**, 121407 (2010).
7. Regan, E. C. et al. Mott and generalized Wigner crystal states in WSe₂/WS₂ moiré superlattices. *Nature* **579**, 359–363 (2020).
8. Tang, Y. et al. Simulation of Hubbard model physics in WSe₂/WS₂ moiré superlattices. *Nature* **579**, 353–358 (2020).
9. Yankowitz, M. et al. Tuning superconductivity in twisted bilayer graphene. *Science* **363**, 1059–1064 (2019).
10. Lu, X. et al. Superconductors, orbital magnets and correlated states in magic-angle bilayer graphene. *Nature* **574**, 653–657 (2019).
11. Nuckolls, K. P. et al. Strongly correlated Chern insulators in magic-angle twisted bilayer graphene. *Nature* **588**, 610–615 (2020).

12. Wu, S., Zhang, Z., Watanabe, K., Taniguchi, T. & Andrei, E. Y. Chern insulators and topological flat-bands in magic-angle twisted bilayer graphene. Preprint at <https://arXiv.org/abs/2007.03735> (2020).
13. Das, I. et al. Symmetry broken Chern insulators and magic series of Rashba-like Landau level crossings in magic angle bilayer graphene. Preprint at <https://arXiv.org/abs/2007.13390> (2020).
14. Sharpe, A. L. et al. Emergent ferromagnetism near three-quarters filling in twisted bilayer graphene. *Science* **365**, 605–608 (2019).
15. Serlin, M. et al. Intrinsic quantized anomalous Hall effect in a moiré heterostructure. *Science* **367**, 900–903 (2020).
16. Kerelsky, A. et al. Maximized electron interactions at the magic angle in twisted bilayer graphene. *Nature* **572**, 95–100 (2019).
17. Xie, Y. et al. Spectroscopic signatures of many-body correlations in magic-angle twisted bilayer graphene. *Nature* **572**, 101–105 (2019).
18. Jiang, Y. et al. Charge order and broken rotational symmetry in magic-angle twisted bilayer graphene. *Nature* **573**, 91–95 (2019).
19. Choi, Y. et al. Electronic correlations in twisted bilayer graphene near the magic angle. *Nat. Phys.* **15**, 1174–1180 (2019); correction **15**, 1205 (2019).
20. Tomarken, S. L. et al. Electronic compressibility of magic-angle graphene superlattices. *Phys. Rev. Lett.* **123**, 046601 (2019).
21. Zondiner, U. et al. Cascade of phase transitions and Dirac revivals in magic-angle graphene. *Nature* **582**, 203–208 (2020).
22. Po, H. C., Zou, L., Vishwanath, A. & Senthil, T. Origin of Mott insulating behavior and superconductivity in twisted bilayer graphene. *Phys. Rev. X* **8**, 031089 (2018).
23. Song, Z. et al. All magic angles in twisted bilayer graphene are topological. *Phys. Rev. Lett.* **123**, 036401 (2019).
24. Ahn, J., Park, S. & Yang, B.-J. Failure of Nielsen-Ninomiya theorem and fragile topology in two-dimensional systems with space-time inversion symmetry: application to twisted bilayer graphene at magic angle. *Phys. Rev. X* **9**, 021013 (2019).
25. Bultinck, N. et al. Ground state and hidden symmetry of magic-angle graphene at even integer filling. *Phys. Rev. X* **10**, 031034 (2020).

26. Kumar, A., Xie, M. & MacDonald, A. H. Lattice collective modes from a continuum model of magic-angle twisted bilayer graphene. Preprint at <https://arXiv.org/abs/2010.05946> (2020).
27. Wu, F. & Das Sarma, S. Collective excitations of quantum anomalous Hall ferromagnets in twisted bilayer graphene. *Phys. Rev. Lett.* **124**, 046403 (2020).
28. Wong, D. et al. Cascade of electronic transitions in magic-angle twisted bilayer graphene. *Nature* **582**, 198–202 (2020).
29. McWhan, D. B. et al. Electronic specific heat of metallic Ti-doped V_2O_3 . *Phys. Rev. Lett.* **27**, 941–943 (1971).
30. Spivak, B. & Kivelson, S. A. Phases intermediate between a two-dimensional electron liquid and Wigner crystal. *Phys. Rev. B* **70**, 155114 (2004).
31. Continentino, M. A., Ferreira, A. S., Pagliuso, P. G., Rettori, C. & Sarrao, J. L. Solid state Pomeranchuk effect. *Physica B* **359–361**, 744–746 (2005).
32. Pustogow, A. et al. Quantum spin liquids unveil the genuine Mott state. *Nat. Mater.* **17**, 773–777 (2018).
33. Saito, Y. et al. Isospin Pomeranchuk effect in twisted bilayer graphene. *Nature* <https://www.nature.com/articles/s41586-021-03409-2> (2021).
34. Kuntsevich, A. Y., Tupikov, Y. V., Pudalov, V. M. & Burmistrov, I. S. Strongly correlated two-dimensional plasma explored from entropy measurements. *Nat. Commun.* **6**, 7298 (2015).
35. Hartman, N. et al. Direct entropy measurement in a mesoscopic quantum system. *Nat. Phys.* **14**, 1083–1086 (2018).
36. Park, J. M., Cao, Y., Watanabe, K., Taniguchi, T. & Jarillo-Herrero, P. Flavour Hund's coupling, correlated Chern gaps, and diffusivity in moiré flat bands. Preprint at <https://arXiv.org/abs/2008.12296> (2020).
37. Chen, S. et al. Electrically tunable correlated and topological states in twisted monolayer-bilayer graphene. *Nature Phys.* **17**, 374–380 (2021).
38. Spivak, B. & Kivelson, S. A. Transport in two dimensional electronic micro-emulsions. *Ann. Phys.* **321**, 2071–2115 (2006).
39. Cao, Y. et al. Strange metal in magic-angle graphene with near Planckian dissipation. *Phys. Rev. Lett.* **124**, 076801 (2020).
40. Polshyn, H. et al. Large linear-in-temperature resistivity in twisted bilayer graphene. *Nat. Phys.* **15**, 1011–1016 (2019).
41. Uri, A. et al. Mapping the twist-angle disorder and Landau levels in magic-angle graphene. *Nature* **581**, 47–52 (2020).

Publisher's note Springer Nature remains neutral with regard to jurisdictional claims in published maps and institutional affiliations.

© The Author(s), under exclusive licence to Springer Nature Limited 2021

Article

Data availability

The data in the main text are available at https://github.com/uzondi/MA_Pomeranchuk.

Code availability

The code used in this work is available at https://github.com/erezberg/pomeranchuk_tblg_theory.

Acknowledgements We thank E. Altman, E. Andrei, E. Khalaf, S. Kivelson, S. Das Sarma, G. Shavit, J. Sulpizio, S. Todadri, A. Uri, A. Vishwanath, M. Zaletel and E. Zeldov for suggestions. E.B. is grateful to A. Young for drawing his attention to the unusual physics near $\nu = \pm 1$, sharing his unpublished data, and for a collaboration on related experimental and theoretical work, proposing that a similar effect to the one discussed here occurs near $\nu = -1$, based on transport measurements. In this work, in contrast, we measured the entropy directly, and mapped the entire phase diagram near $\nu = \pm 1$ using compressibility measurements. Work at Weizmann was supported by a Leona M. and Harry B. Helmsley Charitable Trust grant, ISF grants (numbers 712539 and 13335/16), a Deloro award, the Sagol Weizmann-MIT Bridge programme, the ERC-Cog (See-1D-Qmatter, grant number 647413), the ISF Research Grants in Quantum Technologies and Science Program (grant numbers 994/19 and 2074/19), the DFG (CRC/Transregio 183), the ERC-Cog (HQMAT, grant number 817799), EU Horizon 2020 (LEGOTOP 788715) and the Binational Science Foundation (NSF/BMR-BSF grant number 2018643). Work at MIT was primarily supported by the US Department of Energy (DOE), Office of Basic Energy Sciences (BES), Division of Materials Sciences and Engineering under award DE-SC0001819

(J.M.P.). Help with transport measurements and with data analysis was supported by the National Science Foundation (grant number DMR-1809802), and the STC Center for Integrated Quantum Materials (NSF grant number DMR-1231319) (Y.C.). P.J.-H. acknowledges support from the Gordon and Betty Moore Foundation's EPIQS Initiative through grant GBMF9643 and partial support by the Fundación Ramón Areces. The development of new nanofabrication and characterization techniques enabling this work has been supported by the US DOE Office of Science, BES, under award DE-SC0019300. K.W. and T.T. acknowledge support from the Elemental Strategy Initiative conducted by the MEXT, Japan (grant number JPMXP0112101001), JSPS KAKENHI grant number JP20H00354, and the CREST (JPMJCR15F3), JST. This work made use of the Materials Research Science and Engineering Center Shared Experimental Facilities supported by the National Science Foundation (grant number DMR-0819762) and of Harvard's Center for Nanoscale Systems, supported by the NSF (grant number ECS-0335765).

Author contributions A.R., J.M.P, U.Z., Y.C., P.J.-H. and S.I. designed the experiment. A.R. and U.Z. performed the scanning SET experiments, and J.M.P. and Y.C. performed the monolayer graphene sensing experiments. D.R.-L. and Y.C. fabricated the twisted bilayer graphene devices. A.R., J.M.P, U.Z., Y.C., P.J.-H. and S.I. analysed the data. E.B., Y.O. and A.S. developed the theoretical model. K.W. and T.T. supplied the hBN crystals. A.R., J.M.P, U.Z., Y.C., Y.O., A.S., E.B., P.J.-H. and S.I. wrote the manuscript.

Competing interests The authors declare no competing interests.

Additional information

Supplementary information The online version contains supplementary material available at <https://doi.org/10.1038/s41586-021-03319-3>.

Correspondence and requests for materials should be addressed to E.B., P.J.-H. or S.I.

Peer review information *Nature* thanks Emanuel Tutuc and the other, anonymous, reviewer(s) for their contribution to the peer review of this work.

Reprints and permissions information is available at <http://www.nature.com/reprints>.